8-21-2022

A Dual-Stack Coaxial Magnetic Gear for a Wave Energy Conversion Generator

Hossein Baninajar
Portland State University

Sina Modaresahmadi
University of North Carolina at Charlotte

Ho Yin Wong
Portland State University

Jonathan Z. Bird
Portland State University, jonathanbird@pdx.edu

Wesley B. Williams
University of North Carolina at Charlotte

See next page for additional authors
Follow this and additional works at: https://pdxscholar.library.pdx.edu/ece_fac

Part of the Electrical and Computer Engineering Commons

Let us know how access to this document benefits you.

Citation Details

Authors

Hossein Baninajar, Sina Modaresahmadi, Ho Yin Wong, Jonathan Z. Bird, Wesley B. Williams, Bertrand DeChant, and Parker Southwick

A Dual-Stack Coaxial Magnetic Gear for a Wave Energy Conversion Generator

Hossein Baninajar[1], Sina Modaresahmadi[2], Ho Yin (David) Wong[1], Jonathan Z. Bird[1], Wesley Williams[2], Bertrand DeChant[1], Parker Southwick[1]

[1]Portland State University, Department of Electrical and Computer Engineering, Portland, OR, USA
[2]Department of Engineering Technology, University of North Carolina at Charlotte, Charlotte, NC 28223 USA

This paper presents the electromagnetic and mechanical design and analyses of a 7.67:1 gear ratio magnetic gear for a wave energy converter demonstrator. A 2-D and 3-D magnetostatic finite element analysis (FEA) was conducted to maximize the mass torque density. To increase torque without increasing the diameter a unique dual-stack rotor topology was used along with a twelve-segment per pole-pair inner rotor Halbach array and a four-segment per pole-pair outer rotor Halbach topology. The eddy current loss within the magnetic gear was mitigated by using laminated magnets and a low-loss electrical steel. The experimentally tested magnetic gear had a peak torque of 1796.8 N·m which corresponds to an active region volumetric and mass torque density of 221.1 N·m/L and 105.74 N·m/kg, respectively. The efficiency at rated speed and maximum torque was measured to be 95%. A new in-plane eddy current loss mechanism was identified as being a primary reason for the measured electrical losses being higher than initially calculated.

Index Terms — **Finite element analysis, Magnetic gears, Permanent magnets, Thermal analysis, Wave energy conversion**

I. INTRODUCTION

WAVE energy converters (WEC) are being developed to try to harness the vast energy reserves contained within the ocean's waves. To enable the WEC to be cost competitive the power generation capabilities of the WEC must be designed to be very reliable and require minimal or no maintenance. As the wave motion is periodic and very slow a gearing mechanism is needed to facilitate the use of a more compact high-speed and low-torque generator. As a magnetic gear (MG) creates non-contact torque-speed change, it does not need gear lubrication, and offers unique features, such as inherent overload protection. The use of magnetic gearing offers a potential way of improving a WECs power conversion performance [1-4], and lowering the levelized cost of energy.

Over the past 20+ years various researchers have proposed alternative magnetic gear (MG) topologies. A review of different MG designs is provided in [5, 6]. Due to the coaxial MGs relative simplicity and experimentally demonstrated high torque density, the coaxial radial MG topology has to-date generated the greatest research interest and this type of MG is studied in this paper.

An example of a coaxial MG is shown in Fig. 1. In this embodiment, the inner and outer rotors utilize a four-segment per pole-pair permanent magnet (PM) Halbach rotor topology and the central rotor contains a ferromagnetic lamination stack, with n_c slots. The MG inner and outer rotors contain p_i and p_o pole-pairs. A speed change is created because the inner and outer rotor's PM poles interact with the central ferromagnetic slots to create space harmonics. The spatial and temporal changes in the airgap magnetic field energy simultaneously creates non-contact torque amplification and speed reduction [7, 8]. If the central rotor's ferromagnetic steel slot number is selected to satisfy $n_c = p_i + p_o$ and the outer rotor is held stationary, $\omega_o=0$, the speed ratio will be

$$\omega_i = \omega_c \left(n_c / p_i \right) \tag{1}$$

where ω_i = inner rotor angular speed, and ω_c = central modulation rotor angular speed.
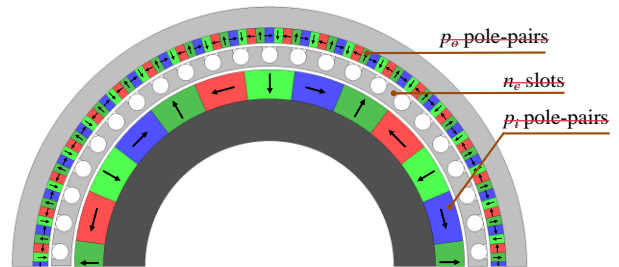

Fig. 1. A half cut-through view of a coaxial MG with (p_i, n_c, p_o) = (6, 46, 40). The inner and outer rotors use a four-segment per pole-pair Halbach rotor permanent magnet topology and the central rotor contains a ferromagnetic lamination stack with n_c slots.

For the design shown in Fig. 1, the gear ratio is $G_r = n_c/p_i = 46/6 = 7.67$.

To create a high torque, the coaxial MG diameter is often increased [9-13], however because of the large part size, as well as the increased difficulty in maintaining a small airgap with a tight tolerance, the use of a large diameter to increase torque will increase the machining costs. The MGs torque can also be increased by extending the MGs axial length. In a PM-generator the increase in torque via an increased axial length is primarily limited by thermal concerns created by electrical loss [14]. However, along with these same thermal concerns the MG also must be designed to mitigate the increased radial deflection on the central ferromagnetic slotted modulator that comes with using a long axial length [15]. In this paper a new type of dual-stack MG design is presented and tested that mitigates the radial deflection concerns by splitting the MG into two axial stacks. This allows the MG torque to be increased without increasing the outer diameter.

The parameter design of the dual-stack MG is focused on maximizing the active region mass torque density rather than the active region volumetric torque density.

The active mass and volumetric torque density, are defined by:

$$T_m = T_e / \left(m_s + m_m \right) \tag{2}$$

$$T_v = T_c / (\pi r_{o6}^2 d_m), \tag{3}$$

respectively, where T_c = torque on the central modulation cage rotor, and m_s = modulation rotor ferromagnetic steel mass, m_m = magnet material mass. And the r_{o6} and d_m are the MG outer radius and axial length, respectively. The design of the MGs that maximize mass torque density has recently been a research focus, especially for use in electric aircraft [16, 17]. Designs that focus primarily on maximizing volumetric torque density tend to lead to MGs with radially long magnets [18] thereby increasing cost. The maximizing of the MG mass torque density leads to a design that has an inner and outer rotor magnet length that is much smaller [19-21], but can still achieve a competitive volumetric torque density.

II. MAGNETIC DESIGN

The 50-kW coaxial MG design requirements are shown in Table I. The chosen MG pole-slot combination is based off a $(p_{bi}, n_{bc}, p_{bo}) = (3, 23, 20)$ base. This combination satisfies:

$$\gcd(2p_{bi}, n_{bc}) = 1, \quad p_{bi} \neq 1. \tag{4}$$

By using an odd number of modulator slots, $n_{bc} = 23$, the torque ripple can be mitigated [22, 23]. However, the odd modulator slot number, will create a large net radial deflection force and this also increases harmonic noise [24]. If the base combination is multiplied by two, giving $(p_i, n_c, p_o) = 2 \times (p_{bi}, n_{bc}, p_{bo})$, the central modulation rotor will then contain an even number of slots, balancing the radial force that is passed to the bearings [25]. And as even harmonic components are not normally present in the rotor field it is shown in this paper that the MG will still have a low torque ripple. In addition, the higher pole-pair number will reduce the field path resulting in a smaller more manageable magnet size.

A summary of the fixed MG geometric and material modeling assumptions used in this paper are shown in Table II and the geometric definitions are shown in Fig. 2. The N-50M magnet grade, with a 100˚C maximum working temperature, was selected for use in the MG design and to mitigate thermal issues, the parameter analysis was conducted when assuming an 80°C magnet temperature. The cage modulation rotor lamination used M-6 material, as this provided a higher saturation level than M-19 and M-27 and this grade also has a lower specific loss [26, 27].

The MG design used a set of non-conductive central modulation circular rods to retain the modulator rotor in place. The circular rods reduced the torque relative to using a rectangular [3, 4, 21, 28, 29], or trapezoidal [30, 31] support rod, but the reduction was determined to be acceptable due to the improved end-plate support mechanism and the lower machining costs associated with using circular rods.

The MG has an 180° symmetry, therefore using 3-D FEA to perform the sizing analysis is computationally challenging. Therefore, to reduce the computational burden, a magnetic scaling analysis was first performed using 2-D FEA. To account for the reduction in torque due to the MG edge-effect [32] an axial edge-factor, k_e, was used. Based on prior experience [29], an edge-factor $k_e = 0.85$ was initially selected. This assumed edge effect factor is later verified by using 3-D FEA analysis, refer

to Table V. The 2-D computed design torque needs to be

$$T_c^{2D} = T_c / (n_s k_e) = 1069 \text{ N·m} \tag{5}$$

where $n_s = 2$ axial stacks. Note that several authors have used lower edge-effect factors, between $k_e = 0.6$ to 0.8 [32], but in this design the airgap is small, and the magnets are radially small. These changes lower the leakage field and improve the MG edge-effect factor.

TABLE I
TARGET SPECIFICATIONS FOR THE STAGE-2 MG

Requirement	Value	Unit
Rated power	50	kW
Output speed, ω_i	2016	r/min
Input rotor torque, T_c	1816	N·m
Output rotor torque, T_i	237	N·m
Gear ratio, $G_r = n_c / p_i$	7.67	-

TABLE II
FIXED MAGNETIC GEAR PARAMETERS

| Parameter	Value
Nd-Fe-B magnet grade, $B_r = 1.415$T	N50M
Laminated rotor steel grade	M6
Magnet working temperature	80°C
Cage rotor bridge thickness, l_b	0.75 mm
Cage rotor upper bridge opening, α_o / α_c	0.85
Inner rotor back iron, l_{ib}	20 mm
Outer rotor back iron, l_{ob}	20 mm
MG axial length, d_m	70 mm
Airgap between rotors, g	0.8mm
Number of MG axial stacks, n_s	2
Cage lamination stacking factor	0.95
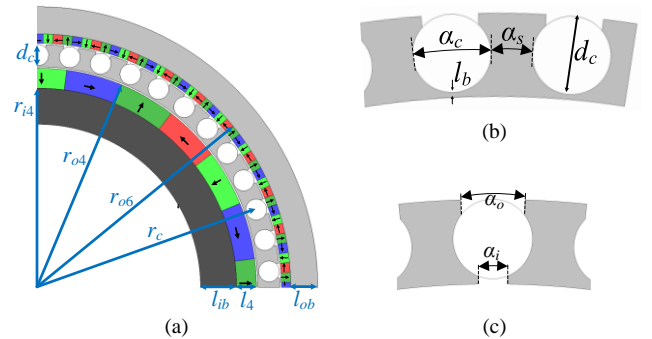
Fig. 2. (a) Radial geometric definitions. (b) Cage rotor geometric definitions used in the sweep analysis of Table III and (c) shows the inner radius separation angle definition used in the sweep analysis used in Fig. 5. The angles are defined relative to the center of the MG.

The design analysis was performed by first conducting a geometric parameter sweep analysis across 4,791 radial lengths as stated in Table III. The inner and outer rotor magnet spans, defined by $\theta_i = \pi/(2p_i)$ and $\theta_o = \pi/(2p_o)$ respectively were kept fixed. The central modulation rotor cage thickness was swept by using a set number of cage rotor rod support diameters, d_c, and outer rotor radius, r_{o6}, values. To ensure the rods are mechanically retained in place the rods upper opening angular span, defined in Fig. 2, was kept fixed, during the sweep analysis, at an angle ratio $\alpha_o = 0.85\alpha_c$, where

$$\alpha_c = 2 \tan^{-1}(d_c / 2r_c) \tag{6}$$

and

$$r_c = r_{o4} + g + d_c / 2 \tag{7}$$

is the center radius of the rod. With a circular rod, the cage rotor ferromagnetic angle span, α_s, is not an independent design parameter, but a function of d_c and r_c.

Fig. 3 shows the computed torque and active mass torque density for each 2-D FEA simulation case. The solid lines show the Pareto front for each outer radius. The peak active region mass torque density for each radius is shown in Table IV.

The active region mass torque density for the $r_{o6} = 140$ mm is 5% higher than for $r_{o6} = 130$ mm but is only 1% lower than for $r_{o6} = 150$ mm. Therefore, the $r_{o6} = 140$ mm design was selected for further study.

To study the impact of the inner rotor radius, a finer step size was then used on the inner radius values. Fig. 4 shows how the mass and volumetric torque density values change for different inner rotor radii, r_{i4}, when $r_{o6} = 140$ mm and r_{i4}, d_c was varied. To create Fig. 4, the sweep values as shown in Table III were used except the cage rod diameter was stepped with a finer 0.5 mm increment. The active region mass and volumetric torque density was computed by evaluating (2) and (3). Note that the outer rotor lamination length, l_{ob}, was not considered in the torque density calculation as it was used to facilitate the outer rotor magnet assembly and not used for torque production purposes.

The designs that have the highest volumetric torque density have small inner radii, r_{i4} and radially long inner rotor magnets. The MG design with $r_{i4} = 110$ mm has the highest mass torque density, and this leads to a relatively short inner rotor magnet length, $l_4 = 21$ mm. From the Fig. 4 analysis results the *Design A*, with the geometric values

$$(r_{i4}, r_{o4}, d_c, r_{o6}) = (110, 121, 11.5, 140) \text{ mm}$$

was selected. *Design A* has a $T_m = 113.6$ N·m/kg active region mass torque density, yielding a torque of $T_c^{2D} = 1085.2$ N·m. The volumetric torque density was calculated to be 251.7 N·m/L. The *Design A* torque metrics are shown in Table V.
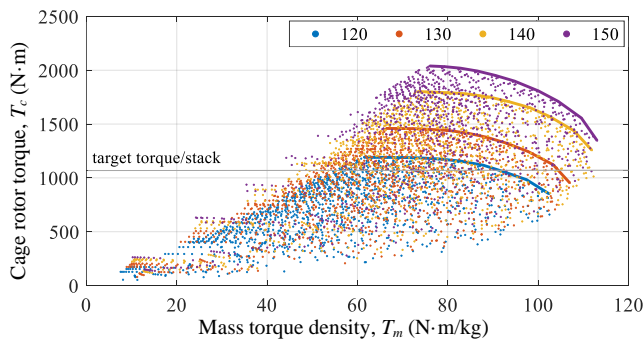
Fig. 3. Torque versus mass torque density for different outer radii. The outer radius value, r_{o6}, is shown in the legend. The solid line shows the Pareto front for each outer radius value.

TABLE III
MAGNETIC GEAR SWEEP PARAMETERS

Description	Sweep values (mm)
Cage rod diameter, d_c	[8, 9, 10, 11, 12]
Outer radius, r_{o6}	120, 130, 140, 150
Inner rotor inner radius, r_{i4}	$[r_{o6}-80, r_{o6}-75, \ldots, r_{o6}-35]$
Inner rotor outer radius, r_{o4}	$[r_{o6}-30, r_{o6}-29, \ldots, r_{o6}-15]$

TABLE IV
2-D FEA COMPUTED PEAK MASS TORQUE DENSITY GEOMETRIC VALUES

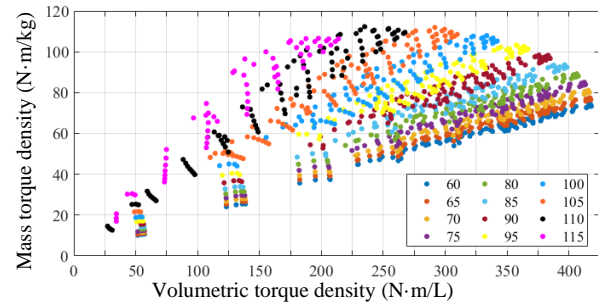| Parameter	Value				Units
Outer radius, r_{o6},	**120**	**130**	**140**	**150**	mm
Inner rotor inner radius, r_{i4}	95	100	110	115	mm
Inner rotor outer radius, r_{o4}	103	112	121	129	mm
Cage rod diameter, d_c	10	10	12	12	mm
Peak mass torque density	102.5	107.1	112.3	113.1	N·m/kg
Torque, T_c^{2D}	852.3	953.2	1012.8	1346.5	N·m

Fig. 4. Parameter sweep results showing the mass and volumetric torque density trade-off when $r_{o6} = 140$ mm. The legend shows the different inner rotor radius r_{i4} values.

TABLE V
SINGLE- STACK MAGNETIC GEAR DESIGN VALUES CALCULATED AT 80ºC

Design	FEA model	Peak torque (N·m)	Torque density		Axial Length (mm)			Back-iron (mm)	Cage angle (degrees)
			(N·m/kg)	(N·m/L)	d_m	d_{cg}	d_o	l_{ob}	α_o
A	2-D	1085	113	251	70	70	70	20	4.36
B	2-D	976	107	226	70	70	70	20	3.5
C	3-D	921	94	197	76	73	76	20	3.5
D	2-D	1055	115	245	70	70	70	20	3.5
	3-D	904	105	222	66	63	66	20	3.5
E	3-D	908	106	223	66	63	33	23	3.5

The cage rotor inner and outer angles, as shown in Fig. 2(c) have a marked impact on the MG performance. A further *Design A* peak torque study was conducted when using different separation angles (α_i, α_o). The separation angles were swept from 0˚ to 5˚, close to the maximum practical separation angle, $\alpha_c = 5.13˚$. The angle span analysis results are shown in Fig. 5. The minimum torque occurs when the inner and outer angles are zero degrees and the maximum torque occurred when the ferromagnetic segments are the maximum separation value: (α_i, α_o) = (5º, 5º). When only the outer angle is maximum, such that (α_i, α_o) = (0º, 5º), the peak torque was 32% higher than the minimum torque value. In contrast, when (α_i, α_o) = (5º, 0º), the peak torque increased by only 2 %. This contrast is due to the small field path created by the outer rotor, relative to the large inner rotor field path [33, 34]. Furthermore, having an inner bridge connection, reduced the torque ripple [34]. Based on this analysis it was decided to utilize (α_i, α_o) = (0º, 3.5º), this is 24% above the torque value when (α_i, α_o) = (0º, 0º). The full separation angle was not used on the outer angle because it would provide less retaining rod mechanical support. Selecting $\alpha_o = 3.5º$ corresponds to a $\alpha_o = 0.73\alpha_c$ ratio. Using these design changes, the 2-D FEA calculated volumetric and mass torque density reduced to 226 N·m/L and 107 N·m/kg, respectively. These new *Design B* values are summarized in Table V and Fig. 2(a) shows the geometric appearance for *Design B*.

This article has been accepted for publication in IEEE Transactions on Magnetics. This is the author's version which has not been fully edited and content may change prior to final publication. Citation information: DOI 10.1109/TMAG.2022.3199580

4

A 3-D axial length sweep analysis was then conducted to give the required axial length per-stack that satisfy the torque requirement ($\geq$ 908 N·m). The selected *Design C* axial stack length for the cage and magnet rotors is shown in Table V. The cage rotor axial length, d_{cg}, is shorter than the magnet axial length, d_m, because it was previously shown that this increased the torque performance by several percent [34, 35].

To further improve the torque and lower the harmonic content a *Design D* MG with a twelve-magnet segment per pole-pair inner Halbach array rotor, as shown in Fig. 6, was used. Fig. 7 shows the reduction in harmonic content that results when using the twelve-magnet segment per pole-pair rotor. The fundamental is increased by 6% and the 5th and 9th harmonics are significantly reduced. The increase in the fundamental field increased the peak torque by 8 % to 1055 N·m. The twelve-magnet segment per pole-pair also reduced the peak-to-peak torque ripple from 0.8 % to 0.6 %.

A 3-D sweep analysis of the *Design D* provided the required axial length when using the twelve-magnet segment per pole-pair Halbach array rotor. The selected *Design D* axial length values and torque performance is shown in Table V.
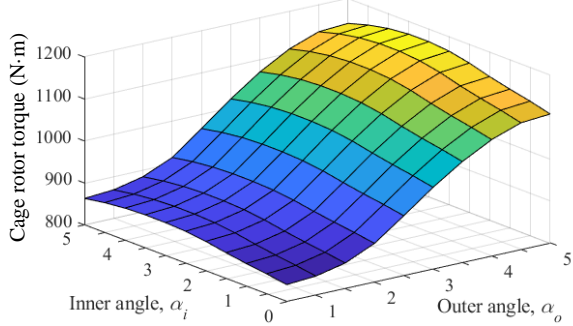

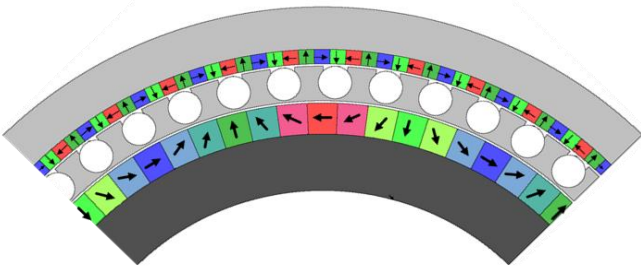Fig. 5. Torque versus separation angles, 2D FEA - d_m = 70 mm.

Fig. 6. The *Design D* magnetic gear with a twelve-magnet segment per pole-pair inner Halbach rotor.
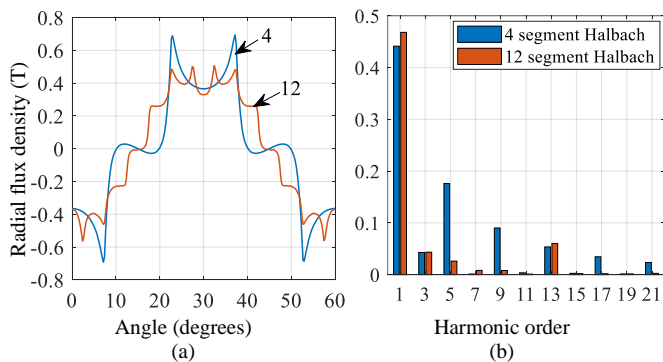

Fig. 7. (a) The inner rotor radial magnetic flux density at r=121.5 mm when the rotor is surrounded by air for the four and twelve-magnet segment per pole-pair Halbach array. (b) shows the corresponding harmonic components with respect to main harmonic. Note that this plot assumes that the magnets are at a working temperature of 80°C.

An outer rotor lamination, like shown in Fig. 6, helped with magnet assembly but reduces the torque [4]. To mitigate torque reduction, an outer rotor lamination that was half the MG axial length $d_o = d_m/2$ was selected. Also, the outer rotor back iron was increased to l_{ob} = 23 mm to provide sufficient mounting bolt hole support. The *Design E* with the outer rotor laminations included is shown in Fig. 8 and the torque values for this *Design E* are shown in Table V.
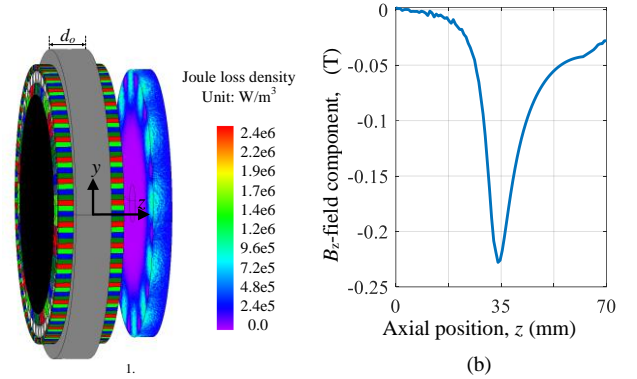

Fig. 8. The *Design E* MG also shown is the contour plot of the joule loss density within the mechanical cage rotor endplate. (b) The B_z-field component change versus axial distance from the center of one stack of the MG at r = 118 mm. The cage rotor endplate is placed at z = 70 mm.

III. MAGNETIC LOSS ANALYSIS

The MG power loss is composed of electrical, magnetic, and bearing loss. Characterizing the frequency of the magnetic field variation in each component gives insight into the severity of the magnetic component loss. The mechanical support within and in close contact to the active region are made of non-magnetic and not conductive material. Therefore, the magnetic loss in the metallic supports, located far away from the active regions, are assumed to be insignificant in the following analysis.

A. Inner Rotor Electrical Harmonics

The inner rotor electrical harmonics can be calculated by considering the modulated field from the outer rotor. Using complex notation, the hth spatially harmonic field distributed from the outer rotor as

$$B_h^o(r,\theta) = B_h(r)e^{jp_o h\theta}, h=1,3,5\ldots \quad (8)$$

The cage rotor ferromagnetic segments will create a set of kth spatial frequency permeance terms described by

$$\lambda_k(r,\theta) = \lambda_k(r)e^{jn_c k\cdot(\theta-\omega_c t)}, k=0, \pm1, \pm3, \pm5\ldots \quad (9)$$

The modulated flux density in the inner rotor airgap can then be described by

$$B_{h,k}^i(r,\theta) = B_h^o(r,\theta)\lambda_k(r,\theta) \quad (10)$$

Substituting (8) and (9) into (10) gives

$$B_{h,k}^i(r,\theta) = B_{h,k}(r)e^{jp_{h,k}(\theta-n_c\cdot\omega_c\frac{k}{p_{h,k}}t)} \quad (11)$$

where

$$B_{h,k}(r) = B_h(r)\lambda_k(r). \quad (12)$$

and the outer rotor spatial harmonic terms are

$$p_{h,k} = hp_o + kn_c. \quad (13)$$

From (11) it can be seen that within the inner rotor airgap the spatial field harmonics will be rotating with a mechanical angular speed of

$$\omega_{h,k} = kn_c \cdot \omega_c \frac{1}{p_{h,k}} . \tag{14}$$

As the inner rotor is rotating with a mechanical angular speed ω_i the spatial harmonics seen be the inner rotor will be rotating with the speed difference:

$$\omega_{h,k}^i = \omega_i - \omega_{h,k} . \tag{15}$$

The electrical frequency seen by the inner rotor is then

$$\omega_{h,k}^{ie} = (\omega_i - \omega_{h,k}) \cdot p_{h,k} \tag{16}$$

Substituting (13) and (14) into (16) gives

$$\omega_{h,k}^{ie} = \omega_i \cdot (p_o h + n_c k) - \omega_c \cdot kn_c \tag{17}$$

Using (1) to rewrite ω_c in terms of ω_i gives

$$\omega_{h,k}^{ie} = \omega_i \cdot p_o h + \omega_i (n_c - p_i) \cdot k \tag{18}$$

Since

$$n_c = p_o + p_i \tag{19}$$

Equation (18) becomes

$$\omega_{h,k}^{ie} = \omega_i \cdot p_o (h + k) . \tag{20}$$

With $p_o = 40$ pole-pairs and $(h,k) = (1,0)$, the fundamental electrical frequency seen by the inner rotor when $\omega_i = 211.1$ rad/s (2016 r/min) is

$$f_{1,0}^{ie} = \omega_{1,0}^{ie} / 2\pi = 1344\,\text{Hz}. \tag{21}$$

B. Outer Rotor Electrical Harmonics

The outer rotor electrical harmonics can be calculated by considering the modulated field from the inner rotor. Defining the mth spatial harmonic field emanating from the inner rotor as

$$B_m^i(r,\theta) = B_m(r)e^{jm \cdot p_i(\theta - \omega_i t)}, \, m = 1,3,5... \tag{22}$$

The modulated magnetic flux density passing to the outer rotor will be

$$B_{m,k}^o(r,\theta) = B_m^i(r,\theta)\lambda_k(r,\theta) \tag{23}$$

Substituting (22) and (9) into (23) gives

$$B_{m,k}^o(r,\theta) = B_{m,k}(r)e^{jp_{m,k}\left[\theta - \frac{m \cdot p_i \cdot \omega_i + k \cdot n_c \cdot \omega_c}{p_{m,k}} \cdot t\right]} \tag{24}$$

where

$$B_{m,k}(r) = B_m(r)\lambda_k(r) \tag{25}$$

and the inner rotor spatial harmonic terms are

$$p_{m,k} = m \cdot p_i + k \cdot n_c . \tag{26}$$

The field emanating from the inner rotor that is present in the outer rotor airgap will be rotating with a mechanical angular speed of

$$\omega_{m,k} = (\omega_i \cdot mp_i + \omega_c \cdot kn_c)\frac{1}{p_{m,k}} \tag{27}$$

and the electrical angular speed is therefore

$$\omega_{m,k}^{oe} = \omega_{m,k} \cdot p_{m,k} . \tag{28}$$

Equation (28) then simplifies to

$$\omega_{m,k}^{oe} = \omega_i \cdot mp_i + \omega_c \cdot kn_c . \tag{29}$$

Utilizing (1) to rewrite ω_c in terms of ω_i gives

$$\omega_{m,k}^{oe} = \omega_i \cdot (m + k)p_i \tag{30}$$

with $p_i = 6$ pole-pairs and $(m,k) = (1,0)$, the fundamental electrical frequency seen by the outer rotor when $\omega_i = 211.12$ rad/s (2016 r/min) is

$$f_{1,0}^{oe} = \omega_{1,0}^{oe} / 2\pi = 201.6\,\text{Hz}. \tag{31}$$

C. Cage Modulator Harmonics

The cage rotor experiences magnetic field variations from both the inner and outer rotors. First, considering the interaction with the inner rotor field interacting with the cage modulator. The mechanical spatial harmonics seen be the cage modulation rotor are described by

$$\omega_{m,k}^c = \omega_{m,k} - \omega_c . \tag{32}$$

The electrical frequency seen by the cage rotor is then

$$\omega_{m,k}^{ce} = (\omega_{m,k} - \omega_c) \cdot p_{m,k} \tag{33}$$

Substituting (26) and (27) into (33) gives

$$\omega_{m,k}^{ce} = \omega_i \cdot mp_i + \omega_c \cdot kn_c - \omega_c \cdot (kn_c + mp_i) . \tag{34}$$

Simplifying and using (1) to write ω_c in terms of ω_i gives

$$\omega_{m,k}^{ce} = \omega_i \cdot mp_i\left[1 - \frac{p_i}{n_c}\right]. \tag{35}$$

Substituting (19) into (35) gives

$$\omega_m^{ce} = m\frac{p_o p_i}{n_c}\omega_i . \tag{36}$$

Using the pole-slot values in (36), the cage rotor fundamental spatial harmonic field frequency ($m = 1$) seen by the rotor is

$$f_1^{ce} = \omega_1^{ce} / 2\pi = 175.3\,\text{Hz}. \tag{37}$$

Lastly, the mechanical angular speed spatial harmonics seen by the cage rotor and due to the outer rotor are

$$\omega_{h,k}^c = \omega^c - \omega_{h,k} \tag{38}$$

where $\omega_{h,k}$ is defined by (14). The electrical frequency seen by the cage rotor is then

$$\omega_{h,k}^{ce} = [\omega_c - \omega_{h,k}] \cdot p_{h,k} . \tag{39}$$

Substituting (13) and (14) into (39) gives

$$\omega_{h,k}^{ce} = \omega_c \cdot [hp_o + kn_c] - \omega_c \cdot k \cdot n_c \tag{40}$$

utilizing (1) to write ω_c in terms of ω_i and simplifying gives

$$\omega_{h,k}^{ce} = h\frac{p_o p_i}{n_c}\omega_i \tag{41}$$

which outputs the same frequency as (36) when $h = 1$. This cage rotor frequency is the lowest rotor frequency within the MG.

There is a trade-off between the calculation time and the accuracy of the loss analysis. Based on the above frequency analysis a time-step of $t_s = 60\mu s$ was selected, this corresponds to a sampling frequency of $f_s = 16.66$ kHz. A 100-step, transient JMAG 3-D FEA simulation was used to compute the steady-state loss values for both stacks of the MG. Due to the axial and

circumferential symmetry the MG FEA model utilized a quarter model of one stack. The calculated component loss comparison, at rated speed, when using solid magnets as well as when using a 2mm thick axially laminated magnet, is shown in Table VI. Note that the laminated magnets were modeled by introducing an insulation condition between each magnet, rather than modeling the actual insulation and adhesive layer length.

The loss was computed by using Steinmetz coefficients and a fast-Fourier transform method [36]. The impact on loss reduction is graphically shown in Fig. 9. The laminated magnets reduced the total MG loss by 3× and therefore the laminated magnets were used in the experimental prototype.

To mitigate edge effect losses the Garolite cage rotor rods were supported using non-conductive Garolite endplates, these non-conductive endplates were then axially supported using a steel-4130 endplate, as shown in Fig. 10(a). To mitigate loss, the conductive endplates were placed 37 mm away from the active region. A plot showing the peak B_z leakage field decay is shown in Fig. 8(b) and Fig. 8(a) shows the eddy current loss density within the end plates when operating the MG at rated speed. The total end-plate loss was computed to be only 18 W (9 W per endplate). To minimize computational burden and as the computed endplate loss was small the thermal analysis neglected the end-plate loss.
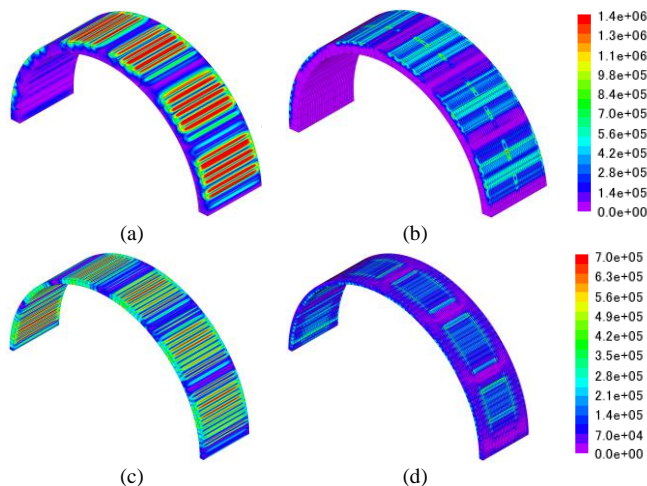

Fig. 9. Contour plot of eddy current density in A/m^2 at ω_i = 2016 r/min and maximum torque, for (a) solid inner rotor magnets, (b) laminated inner rotor magnets, (c) solid outer rotor magnets, and (d) laminated outer rotor magnets.

IV. THERMAL ANALYSIS

Using the active region loss values shown in Table VI, a 3-D steady-state thermal analysis was completed to capture the thermal pathways within the MG and to predict temperature ranges. The thermal analysis was completed by using the half-symmetry MG mechanical design, as shown in Fig. 10(a). The thermal conductivity of each material used in the thermal analysis is shown in Table VII. The MG rotors were supported using end-plates made of Garolite G-11. This material is a good thermal insulator. Air geometry regions were added to the internal cavity of the MG model via a Boolean method within ANSYS's native CAD software, SpaceClaim.

The thermal analysis was completed by assuming that the surrounding medium was at 20°C with an initial MG temperature of 22°C. The model assumptions were selected so as to

show that even in an environment with minimal external cooling, such as in a laboratory space, the MG will not exceed the magnet operating temperature, ≤ 100°C.

Fig. 10 shows the FEA computed thermal distribution within the MG when applying a single convective outer boundary heat transfer coefficient value of h = 10 W/m^2·K. The maximum temperature of the MG was calculated to be 73.7°C and the peak temperature occurred near the inner magnets and cage laminations. The average temperature of each active region MG component is summarized in Fig. 11.
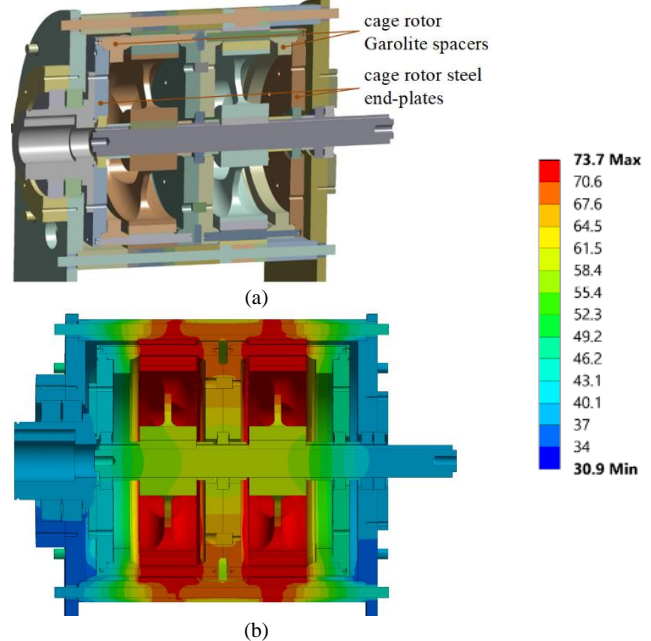

Fig. 10. (a) Isometric mid-sectional view of the geometry used for the steady-state thermal analysis of the MG. The axial gap between stacks is 60 mm. (b) Mid-sectional view of the computed MG temperature at ω_i = 2016 r/min and maximum torque for h = 10 (W/m^2·K).

TABLE VI
ACTIVE REGION COMPONENT LOSS AT RATED SPEED

Description	Loss (W)		Laminated Loss density (W/m^3)
	Solid magnets	Laminated magnets	
Inner magnet Joule loss†	269	38.4	29,297
Inner back-iron loss	2.4	2.4	3,435
Cage rotor Joule loss*	46.8	46.8	106,890
Cage rotor Hysteresis loss	21.8	21.8	
Outer magnet Joule loss†	151	19.6	34,065
Outer back iron Joule loss*	33.8	33.8	37,536
Outer back iron hysteresis loss	19.2	19.2	
Total active region electrical loss	544	182	

* Only includes loss due to parallel fields to laminations
† Includes loss from parallel and perpendicular field components

TABLE VII
THERMAL CONDUCTIVITY

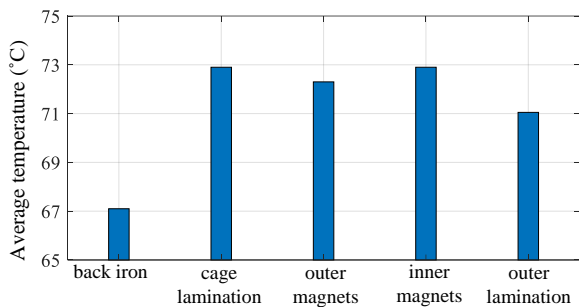| Region	Description	Value (W/m·K)
Active region	Airgap areas	0.026
	Cage rotor Garolite rods and end plates	0.3
	Cage rotor and outer rotor laminations	28
	Inner and outer rotor magnets	7.6
Structural regions	Outer rotor endplates (Aluminum)	237.5
	Cage end-plate (4130 Steel)	42.7
	Inner rotor core and outer rods(Carbon Steel)	54
	Outer rotor insulation inserts (Delrin)	0.3

Fig. 11. The thermal analysis calculated average temperature for each heat generating active region component.

V. FORCE AND DEFLECTION ANALYSIS

The cage rotor laminations were mechanically supported by the $n_c = 46$ Garolite G11 circular rods. The electromagnetic force experienced by each Garolite rod was computed by evaluating the force between the two blue lines as shown in Fig. 12. The total force on the nth Garolite rod is described by

$$\mathbf{F}_c(n) = F_r(n)\widehat{\mathbf{r}} + F_\theta(n)\widehat{\boldsymbol{\theta}}. \tag{42}$$

Fig. 13 shows the 2-D FEA calculated radial and tangential force on each Garolite rod. Note that due to 180° symmetry, the total radial force summed to zero. The 2-D FEA calculated electromagnetic force values were applied to the 3-D ANSYS deflection model, therefore neglecting the field reduction at the axial ends, the applied force values will be higher than expected, and this provides an additional safety margin.

The approach employed for the structural analysis of the MG is sub-system isolation, meaning that the cage rotor is simulated separately. This is while the forces generated in the presence of the other rotors' magnetic field are applied to the cage rotor. The laminated structure of magnetic steel pieces used in the cage rotor is a critical factor in the deflection analysis, as they show much lower strength compared to the solid steel bars. Based on the static deflection experiments conducted in [37] a bonding agent laminated stiffness factor of 1.15×10^{-4} (unitless) between each lamination was utilized in the 3-D static ANSYS structural analysis model in which each individual lamination was modelled.
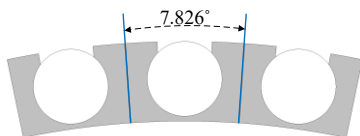

Fig. 12. The electromagnetic force on each Garolite bar was computed by evaluating the force applied on the ferromagnetic segments between each two blue lines.
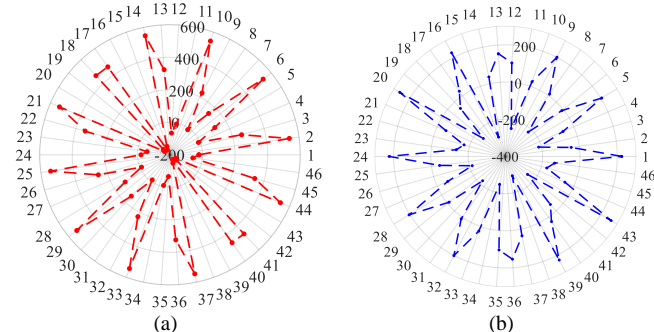

Fig. 13. The calculated (a) radial force, F_r (N), and (b) tangential force, F_θ, (N) on each of the 46 Garolite support rods.

Fig. 14 shows the computed deflection of the cage rotor components when the force shown in Fig. 13 was applied to each Garolite rod. The contour plot of the displacement shows a maximum airgap reduction of 15%. As the criterion set for a failed structure was an airgap reduction of 50% this design was deemed acceptable.
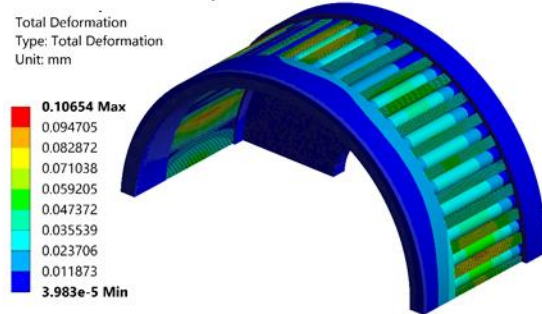

Fig. 14. The half-symmetry ANSYS structural model in which all the laminations are individually modelled. The contour plot shows the deflection is maximum near the axial center.

VI. EXPERIMENTAL VERIFICATION

All six MG rotors were fabricated separately. The outer rotors' four-segment per pole-pair magnet assembly sequence followed the assembly steps explained in [4]. In [4] the outer rotor laminations had slots to locate the radial magnets. These slots however reduced the performance by introducing leakage flux paths. To avoid using a slotted magnet design, a slotted magnet locating assembly jig, shown in Fig. 15(a), was used. After bonding the radial magnets to the outer rotor housing, no assembly jig was then needed for assembling the tangential magnets. The partially complete insertion process for the tangential magnets is shown in Fig. 15(b).

To deal with magnet tolerance inaccuracies, a negative tolerance was defined.

The inner rotor magnet assembly was performed by first populating the 72 plastic shims in place of the magnets between the inner rotor assembly jig and the inner rotor back-iron, then replacing the shims with magnets in three steps, the three assembly steps are numbered in Fig. 16. Fig. 17 shows the fully assembled inner and outer rotor.
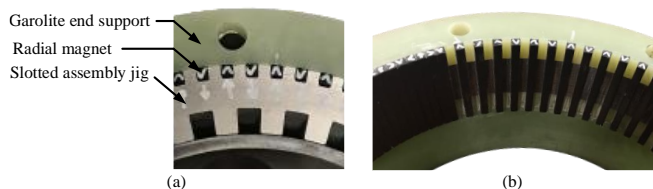

Fig. 15. Slotted outer rotor magnet assembly jig, (b) slots between radial magnets for tangential magnets assembly.

A. Rotor Field Measurements

The inner and outer rotor radial magnetic flux density comparison between the measured and the FEA model is shown in Fig. 18. The inner and outer rotor measured fundamental field was 4 % and 8 % lower than the FEA calculated value, respectively. This reduction is believed to be due to neglecting the magnet stacking factor, insulated and adhesive layers between each magnet stack, in the FEA model. This made the total magnet material thickness to be ~ 2% smaller than total magnets

This article has been accepted for publication in IEEE Transactions on Magnetics. This is the author's version which has not been fully edited and content may change prior to final publication. Citation information: DOI 10.1109/TMAG.2022.3199580

8

mechanical thickness. Also, the manufactured outer rotor magnets were undersized by 0.1 mm along azimuthal direction this also introduced a reduction in the flux density.

After reducing the inner and outer rotor magnet residual flux density to $B_{ri} = 1.36$ T and $B_{ro} = 1.31$ T respectively, the fundamental field components calculated using FEA matched. Using these residual flux density values the FEA computed peak static torque, at an 80°C working temperature, reduced to 1,616 N·m, an 11 % reduction. The MG temperature plays an important role in MG performance, for example at a 20°C working temperature the peak static torque increased by 18% to 1901 N·m.
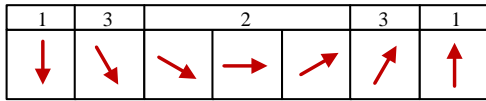

Fig. 16. The three-step numbered sequence used for bonding the inner rotor magnets to the inner rotor housing is shown.
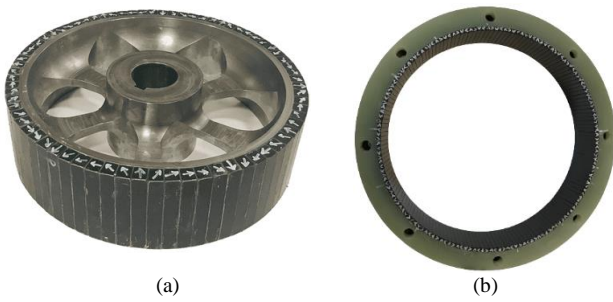

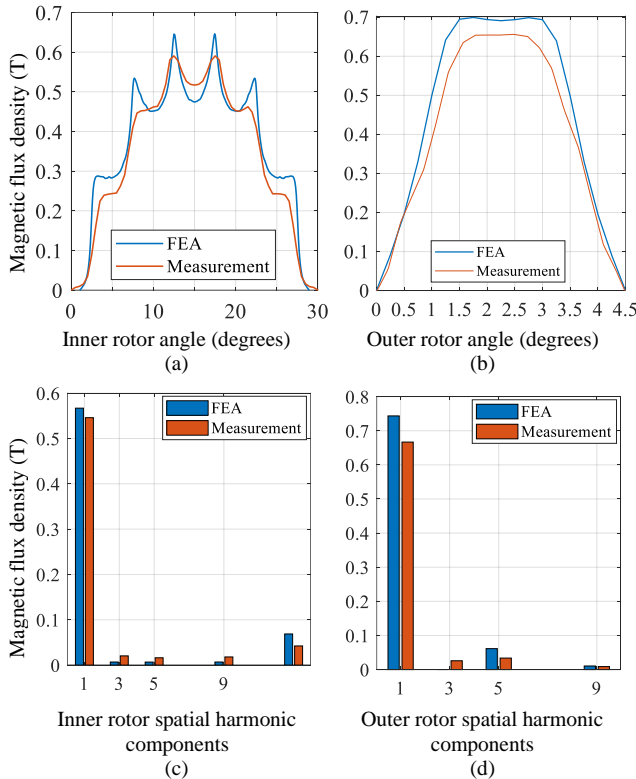Fig. 17. Fully magnet populated (a) inner rotor, (b) outer rotor.

Fig. 18. Comparison between the experimental and calculated magnetic flux density in (a) inner rotor airgap and (b) outer rotor airgap. (c) and (d) show the corresponding spatial harmonics for the inner and outer rotors fields. The measurements were taken at the axial center of the rotor and 0.9 mm above the magnet surface. The ambient temperature was ~ 20°C.

B. Rotor Assembly

The first inner rotor was nested into the corresponding cage rotor as shown in Fig. 19(a). The inner rotor was then slid into the cage rotor while keeping the cage rotor concentric to the shaft. After completing the assembly of the inner rotor of the second stack using the same method as shown in Fig. 19(b), the final assembly of the MG was performed by arranging the rotors as shown in Fig. 19(c). The two outer rotors were pushed together. The outer rotor rods shown in Fig. 19(c) ensured concentricity of the two rotors during assembly.

The assembled MG on the test setup is shown in Fig. 20. The high-speed shaft of the MG was driven by a 55 kW Yaskawa AC servo motor (model SGMBH-5EDCAL), while the low-speed shaft was connected to the 56 kW Marathon induction motor (Part # 365TSTDBD6060) via the 11:1 Sumitomo gearbox. Both the input and output torque and angular speeds were measured using the Himmelstein torque transducers.
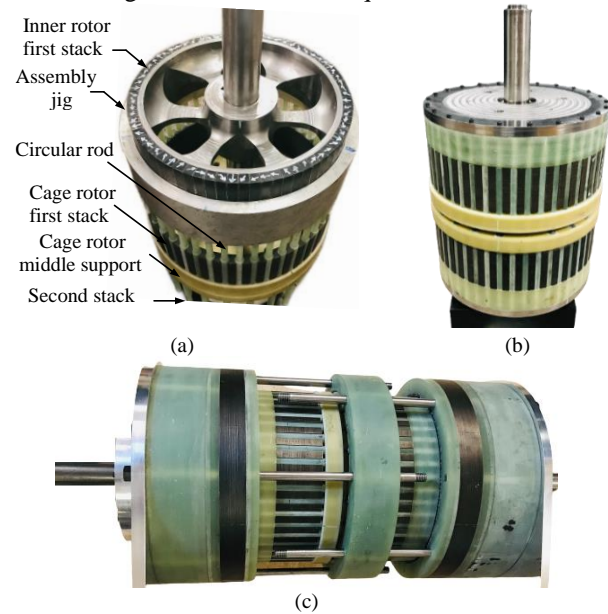

Fig. 19. (a) Inserting inner rotor into the cage rotor, (b) two-stack inner-cage rotor fully assembled, (c) arrangement for sliding the outer rotors over the inner-cage sub-assembly.

The peak static cage rotor torque was measured by locking the inner rotor shaft and applying the torque on the high-torque shaft till pole slipping occurred. The measured peak static torque was $T_c = 1796.8$ N·m. This is a 5 % reduction relative to the calculated torque at 20°C. This reduction was believed to be due to rotor phase shifting between the MG stacks and also could be caused by laminated material discrepancies. It should be noted that the mechanical support between stacks is 60 mm. This stack length was not optimized, however, if this stack length was included into the active region torque density calculation the torque density for the MG would decrease from analysis the MGs volumetric torque density would reduce from 221 N·m/L to 147.4 N·m/L.
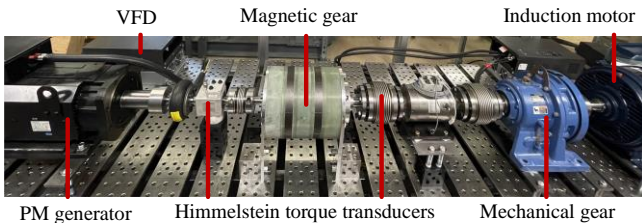
This article has been accepted for publication in IEEE Transactions on Magnetics. This is the author's version which has not been fully edited and content may change prior to final publication. Citation information: DOI 10.1109/TMAG.2022.3199580

9

Fig. 20. The complete assembled stage-2 magnetic gear on the test-stand.

C. Torque and Torque Ripple

Fig. 21 shows the measured torque as a function of time during load torque step changes when the inner rotor angular speed is $\omega_i = 105$ r/min. This plot shows the low torque ripple when the MG is under load and connected to the induction motor. Fig. 22 shows the no-load torque ripple at $\omega_i = 300$ r/min, when the MG was driven by the PM motor. It can be noted that the torque ripple is very low.
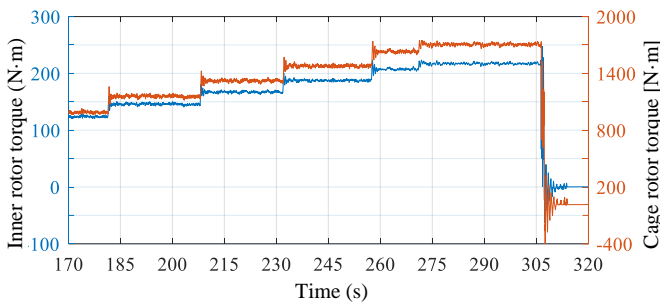

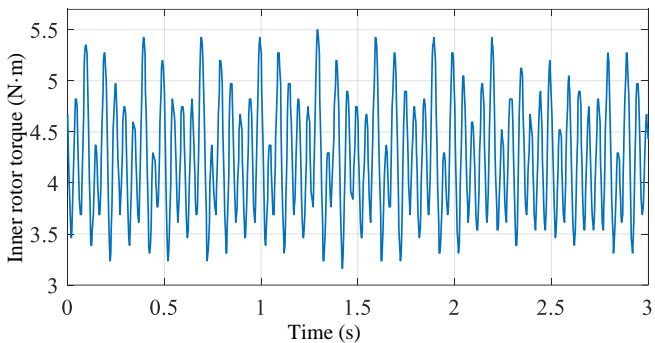Fig. 21. Measured torque at inner rotor speed of 105 r/min at different load.

Fig. 22. Measured inner rotor torque at no-load condition when $\omega_i = 300$ r/min.

D. Loss Measurements

The loss within the MG was measured under no-load by disconnecting the cage modulation rotor from the induction generator and sweeping the inner rotor speed from zero to the rated speed, $\omega_i = 2,016$ r/min. The measured loss as a function of input speed is shown in Fig. 23. The average measured torque, T_i, was used to compute the power loss:

$$P_L(\omega_i) = T_i \omega_i \qquad (43)$$

By curve-fitting the measured loss, the loss can be accurately modeled using

$$P_L(\omega_i) = 0.5 \cdot \omega_i + 0.00024 \cdot \omega_i^2 \qquad (44)$$

The torque model curve fit is shown in Fig. 23. The measured loss at the rated speed is 1983 W. This was 3.4× higher than the 581W active region computed loss (399 W mechanical rolling friction loss and 182W in electrical loss). It was determined that

some of the loss discrepancy can be accounted for by further examining the loss within the structural components. For example, studying the thermal image shown in Fig. 24, that was taken just after completing the loss analysis, it can be noted that there is a significant heating occurring near the outer rotor supports and outer laminations. This heating was determined to be caused by in-plane eddy current loss within the laminations and support rods. These two loss mechanisms are studied in the next two sections.
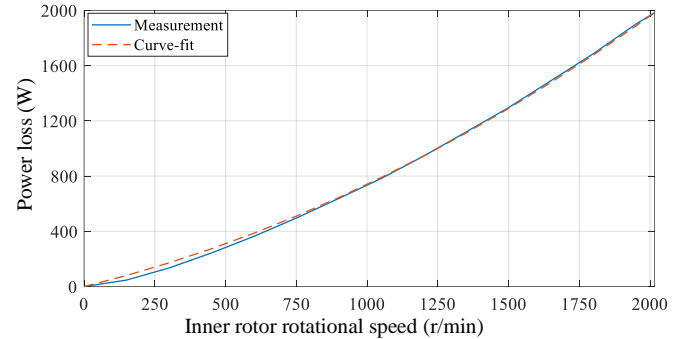

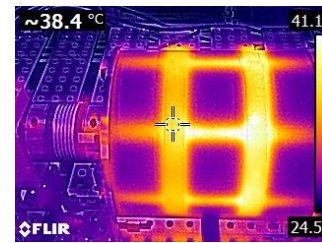Fig. 23. Measured power loss of the MG as a function of inner rotor speed.

Fig. 24. Thermal-image of the MG *after* the loss measurement experiment.

E. Outer Rotor Rod Support Joule Loss

In the prior simulation analysis, the low carbon steel support rods were not included as it was thought that the rods' magnetic (higher reluctance relative to laminated material) properties would shield the losses. However, the contour plot of the joule loss density shown in Fig. 25 shows that significant loss is present in the rods. At rated speed this loss was computed to be 240W. A significant proportion of this unaccounted loss was caused by the axial B_z field within the conductive rods. For example, Fig. 26 shows the vector plot of the induced current density within one single outer rotor rod along with the inner rotor B_z-field component along the rod. The high loss density within the rod is caused by the time-changing axial B_z field component, causing circulating circumferentially directed eddy current loss flow, these circulating currents are shown as red vectors in Fig. 26. The purple eddy current density vectors shown in the middle of Fig. 26 are flowing in the z-axis direction and these currents are caused by the much lower B_r field component within the rod.

F. In-Plane Eddy Current Lamination Loss

The perpendicular, B_z, magnetic flux density component is large in the MG end-regions. Prior loss analysis neglected this axial field loss mechanism. However, the in-plane eddy current loss was determined to be significant. For example, The JMAG 3-D FEA computed in-plane eddy current vectors within the cage

This article has been accepted for publication in IEEE Transactions on Magnetics. This article is the author's version which has not been fully edited and content may change prior to final publication. Citation information: DOI 10.1109/TMAG.2022.3199580

10

and outer rotor laminations are shown in Fig. 27. The in-plane eddy current loss within the outer rotor and cage rotor was computed to be 366W and 35W respectively. Fig. 28 shows that by making the outer rotor laminations short this led to an increase in outer rotor eddy current loss.

G. Efficiency

Table VIII summarizes the total calculated loss values as well as the measured loss. The discrepancy between the measured and calculated loss has reduced to being 37 % higher. The no-load power loss measurements provided a means of characterizing the efficiency. Applying the speed ratio between the inner and cage rotors as given by (1), the curve fitted loss in (44) with respect to the cage rotor angular speed is

$$P_L(\omega_c) = 0.5G_r \cdot \omega_c + 0.00024G_r^2 \cdot \omega_c^2. \qquad (45)$$

And the MG efficiency is computed using

$$\eta(\omega_c, T_c) = 1 - \frac{P_L(\omega_c)}{T_c\omega_c}. \qquad (46)$$

Using (46) the efficiency map, as shown in Fig. 29 was created. Despite the higher-than-expected loss, the MG still provides a relatively high efficiency of 95% when operating at full-load and rated speed $(T_c, \omega_c) = (1796 \text{ N·m}, 263 \text{ r/min})$. Note that the efficiency map does not account for slip torque reduction due to elevated temperature. This only affects the efficiency near the peak torque.
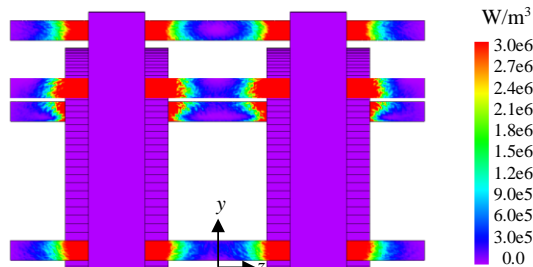

Fig. 25. Joule loss density induced within the outer rotor rods. Due to symmetry, only half of the MG (at $y > 0$) is shown.
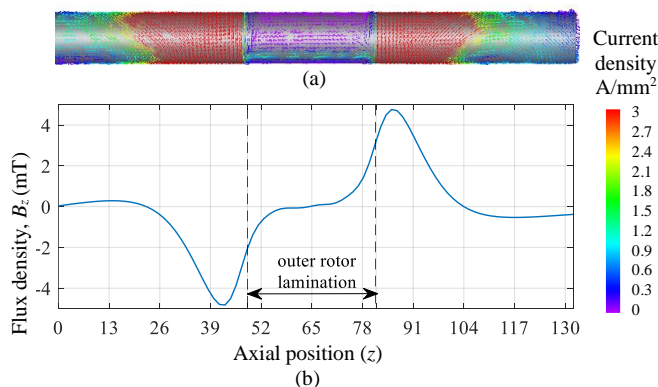

Fig. 26. (a) Outer rotor rod current density vector plot. Due to symmetry, only half of the rod, $z > 0$ is shown. The large loss is caused by the circumferential directed eddy currents. (b) The variation of the inner rotor B_z-field component at $r = 151.5$ mm (center of rod cross section). The outer rotor B_z-field was excluded from the plot.
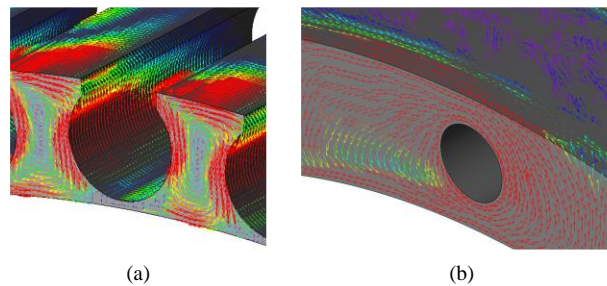

Fig. 27. Presentation of the in-plane eddy current density vectors within (a) cage and (b) outer rotor laminations. The circulating in-plane eddy current is evident.
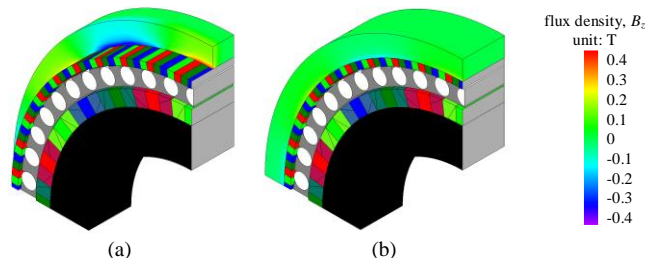

Fig. 28. Half cut-through view showing the B_z-field within the outer rotor laminations when (a) the outer rotor contains the same magnet and lamination axial length. (b) The outer rotor lamination axial length is half of the magnet axial length.

TABLE VIII
CALCULATED LOSS AT RATED SPEED

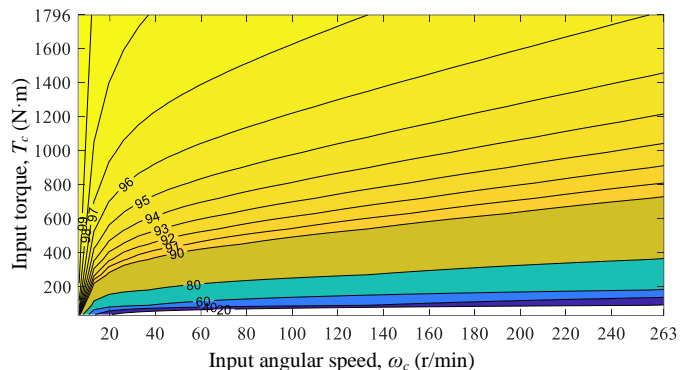| Description	Value (W)
Active-region magnet and lamination loss	182
In-plane cage rotor joule loss	35
In-plane outer rotor lamination joule loss	366
Outer rotor rod joule loss	240
Cage rotor end-plate joule loss	18
Bearing rolling friction loss	399
Total calculated loss	1,240
Measured loss	1,983

Fig. 29. Contour plot of efficiency with angular speed and applied torque

VII. CONCLUSION

This paper has presented a magnetic and mechanical design as well as the experimental testing results for a 7.67:1 dual-stack MG. The dual-stack MG had a measured peak torque of 1796.8 N·m which corresponds to an active region volumetric and mass torque density of 221 N·m/L and 105 N·m/kg, respectively. The rated efficiency was measured to be 95%. The use of laminated magnets was shown to significantly lower MG

loss. However, it was also identified, for the first time, that the in-plane eddy current loss, caused by the axial B_z-field component significantly increased the loss within the MG. Note that not including these additional heat sources which were calculated afterwards is a limit to the thermal model in section IV. Also, it was shown that the use of an axially shorter outer rotor lamination stack increases the edge effect field and significantly increase the in-plane eddy current loss within the MG.

ACKNOWLEDGMENTS

REFERENCES

[1] B. McGilton, R. Crozier, A. McDonald, and M. Mueller, "Review of magnetic gear technologies and their applications in marine energy," *IET Renewable Power Generation,* vol. 12, no. 2, pp. 174-181, 2018.

[2] J. Z. Bird, "Magnetically Geared Rotary Generators for Marine Hydrokinetic Power Take-Off – A Status Update," in *OCEANS 2019 - Marseille*, 17-20 June 2019 2019, pp. 1-7.

[3] H. Baninajar, J. Z. Bird, S. Modaresahmadi, and W. Williams, "Electromagnetic and mechanical design of a hermetically sealed magnetic gear for a marine hydrokinetic generator," presented at the IEEE Energy Conv. Cong. Expo., Portland, OR, 2018.

[4] H. Baninajar, J. Z. Bird, S. Modaresahmadi, and W. Williams, "Electromagnetic Design and Assembly Analysis of a Halbach Rotor Magnetic Gear for a Marine Hydrokinetic Application," in *2019 IEEE Energy Conversion Congress and Exposition (ECCE)*, 29 Sept.-3 Oct. 2019 2019, pp. 732-739.

[5] K. Li and J. Z. Bird, "A review of the volumetric torque density of rotary magnetic gear designs," presented at the XIII Intern. Conf. Electrical Machines, Alexandroupoli, 2018.

[6] B. Praslicka, M. C. Gardner, M. Johnson, and H. A. Toliyat, "Review and Analysis of Coaxial Magnetic Gear Pole Pair Count Selection Effects," *IEEE Journal of Emerging and Selected Topics in Power Electronics,* pp. 1-1, 2021.

[7] K. Atallah and D.Howe, "A Novel High-Performance Magnetic Gear," *IEEE Trans. Magn. ,* vol. 37, no. 4, pp. 2844 - 2846 2001.

[8] B. Ackermann and L. Honds, "Magnetic drive arrangement comprising a plurality of magnetically cooperating parts which are movable relative to one another," U.S. Patent 5,633,555, 1997.

[9] K. Li, S. Modaresahmadi, W. B. Williams, J. D. Wright, D. Som, and J. Z. Bird, "Designing and Experimentally Testing a Magnetic Gearbox for a Wind Turbine Demonstrator," *IEEE Transactions on Industry Applications,* vol. 55, no. 4, pp. 3522-3533, 2019.

[10] S. N. Udalov, A. A. Achitaev, and A. G. Pristup, "Investigations of a magnetic gear for application in wind turbines," in *2016 11th International Forum on Strategic Technology (IFOST)*, 1-3 June 2016 2016, pp. 166-171.

[11] H. Polinder, J. A. Ferreira, B. B. Jensen, A. B. Abrahamsen, K. Atallah, and R. A. McMahon, "Trends in Wind Turbine Generator Systems," *IEEE Journal of Emerging and Selected Topics in Power Electronics,* vol. 1, no. 3, pp. 174-185, 2013.

[12] M. Desvaux, R. L. G. Latimier, B. Multon, H. B. Ahmed, and S. Sire, "Design and optimization of magnetic gears with arrangement and mechanical constraints for wind turbine applications," in *2016 Eleventh International Conference on Ecological Vehicles and Renewable Energies (EVER)*, 6-8 April 2016 2016, pp. 1-8.

[13] A. Penzkofer and K. Atallah, "Magnetic Gears for High Torque Applications," *IEEE Trans. Magn.,* vol. 50, no. 11, p. Article# 8104704 2014.

[14] E. Gundabattini, A. Mystkowski, A. Idzkowski, R. S. R., and D. G. Solomon, "Thermal Mapping of a High-Speed Electric Motor Used for Traction Applications and Analysis of Various Cooling Methods—A Review," *Energies,* vol. 14, no. 5, p. 1472, 2021.

[15] K. K. Uppalapati and J. Z. Bird, "An Iterative Magnetomechanical Deflection Model for a Magnetic Gear," *Magnetics, IEEE Transactions on,* vol. 50, no. 2, pp. 245-248, 2014.

[16] M. C. Gardner, B. Praslicka, M. Johnson, and H. A. Toliyat, "Optimization of Coaxial Magnetic Gear Design and Magnet Material Grade at Different Temperatures and Gear Ratios," *IEEE Transactions on Energy Conversion,* vol. 36, no. 3, pp. 2493-2501, 2021.

[17] J. J. Scheidler, V. M. Asnani, and T. F. Tallerico, "NASA's Magnetic Gearing Research for Electrified Aircraft Propulsion," in *2018 AIAA/IEEE Electric Aircraft Technologies Symposium (EATS)*, 12-14 July 2018 2018, pp. 1-12.

[18] K. K. Uppalapati, J. Z. Bird, J. Wright, J. Pitchard, M. Calvin, and W. Williams, "A magnetic gearbox with an active region torque density of 239Nm/L," *IEEE Trans. Ind. Appl.,* vol. 54, no. 2, pp. 1331-1338, April 2018.

[19] T. F. Tallerico, J. J. Scheidler, and Z. A. Cameron, "Electromagnetic Mass and Efficiency of Magnetic Gears for Electrified Aircraft," in *2019 AIAA/IEEE Electric Aircraft Technologies Symposium (EATS)*, 22-24 Aug. 2019 2019, pp. 1-25.

[20] T. F. Tallerico, Z. A. Cameron, and J. J. Scheidler, "Design of a Magnetic Gear for NASA's Vertical Lift Quadrotor Concept Vehicle," in *2019 AIAA/IEEE Electric Aircraft Technologies Symposium (EATS)*, 22-24 Aug. 2019 2019, pp. 1-21.

[21] H. Y. Wong, H. Baninajar, B. Dechant, and J. Bird, "Designing a Magnetic Gear for an Electric Aircraft Drivetrain," in *2020 IEEE Energy Conversion Congress and Exposition (ECCE)*, 11-15 Oct. 2020 2020, pp. 1-6.

[22] N. W. Frank and H. A. Toliyat, "Gearing ratios of a magnetic gear for marine applications," in *2009 IEEE Electric Ship Technologies Symposium*, 20-22 April 2009 2009, pp. 477-481.

[23] D. C. Hanselman, "Effect of skew, pole count and slot count on brushless motor radial force, cogging torque and back EMF," *IEE Proceedings - Electric Power Applications,* vol. 144, no. 5, pp. 325-330.

[24] S. S. Nielsen, H. Y. Wong, H. Baninajar, J. Z. Bird, and P. O. Rasmussen, "Pole and Segment Combination in Concentric Magnetic Gears: Vibrations and Acoustic Signature," *IEEE Transactions on Energy Conversion,* pp. 1-1, 2022.

[25] C. Agenbach, D. N. J. Els, R. Wang, and S. Gerber, "Force and vibration analysis of magnetic gears," *XIII Intern. Conf. Elect. Mach,* 2018.

[26] O. Chirino and C. Jordan, "Magnetomechanical Applications Utilizing Silicon Iron," *IEEE Transactions on Component Parts,* vol. 12, no. 1, pp. 11-16, 1965.

[27] R. P. Krause, J. H. Bularzik, and H. R. Kokal, "A pressed soft magnetic material for motor applications," in *IEE Half-Day Colloquium on New Magnetic Materials - Bonded Iron, Lamination Steels, Sintered Iron and Permanent Magnets (Digest NMo. 1998/259)*, 28-28 May 1998 1998, pp. 2/1-2/4.

[28] M. Desvaux, B. Multon, H. B. Ahmed, and S. Sire, "Magneto-mechanical analysis of magnetic gear pole pieces ring from analytical models for wind turbine applications," *Wind Engineering,* vol. 42, no. 4, pp. 276-285, 2018/08/01 2018.

[29] H. Baninajar, S. Modaresahmadi, H. Y. Wong, J. Z. Bird, W. Williams, and B. Dechant, "Designing a Halbach Rotor Magnetic Gear for a Marine Hydrokinetic Generator " *Submitted to IEEE Transactions on Energy Conversion* 2022.

[30] D. J. Evans and Z. Q. Zhu, "Novel Partitioned Stator Switched Flux Permanent Magnet Machines," *IEEE Transactions on Magnetics,* vol. 51, no. 1, pp. 1-14, 2015.

[31] Z. A. Cameron, T.Tallerico, and J. J. Scheidler, "Lessons Learned in Fabrication of a High-Specific-Torque Concentric Magnetic Gear," presented at the e Vertical Flight Society 75th Annual Forum & Technology Display, Philadelphia, Pennsylvania, May 13–16, 2019, 2019.

[32] S. Gerber and R. Wang, "Analysis of the end-effects in magnetic gears and magnetically geared machines," in *2014 International Conference on Electrical Machines (ICEM)*, 2-5 Sept. 2014 2014, pp. 396-402.

[33] Y. Zhan, L. Ma, K. Wang, H. Zhao, G. Xu, and N. Ding, "Torque Analysis of Concentric Magnetic Gear With Interconnected Flux Modulators," *IEEE Transactions on Magnetics,* vol. 55, no. 6, pp. 1-4, 2019.

[34] M. C. Gardner, M. Johnson, and H. A. Toliyat, "Performance Impacts of Practical Fabrication Tradeoffs for a Radial Flux Coaxial Magnetic Gear with Halbach Arrays and Air Cores," in *2019 IEEE Energy Conversion Congress and Exposition (ECCE)*, 29 Sept.-3 Oct. 2019 2019, pp. 3129-3136.

[35]   H. Y. Wong, J. Z. Bird, D. Barnett, and W. Williams, "A High Torque Density Halbach Rotor Coaxial Magnetic Gear," in *2019 IEEE International Electric Machines & Drives Conference (IEMDC)*, 12-15 May 2019 2019, pp. 233-239.

[36]   "Improvements in Accuracy of Anomalous Eddy Current Loss Calculations," *JMAG White paper,* 2018. [Online]. Available: https://www.jmag-international.com/wp-content/uploads/members/en/whitepaper/W-MA-88_en.pdf.

[37]   S. Modaresahmadi, D. Barnett, H. Baninajar, J. Z. Bird, and W. B. Williams, "Structural modeling and validation of laminated stacks in magnetic gearing applications," *International Journal of Mechanical Sciences,* vol. 192, p. 106133, 2021/02/15/ 2021.